

Original citation:

Brady, Christopher S. and Arber, Tony. (2016) Simulations of Alfvén wave driving of the solar chromosphere - efficient heating and spicule launching. *Astrophysical Journal*, 829 (2). 80.

Permanent WRAP URL:

<http://wrap.warwick.ac.uk/81268>

Copyright and reuse:

The Warwick Research Archive Portal (WRAP) makes this work by researchers of the University of Warwick available open access under the following conditions. Copyright © and all moral rights to the version of the paper presented here belong to the individual author(s) and/or other copyright owners. To the extent reasonable and practicable the material made available in WRAP has been checked for eligibility before being made available.

Copies of full items can be used for personal research or study, educational, or not-for-profit purposes without prior permission or charge. Provided that the authors, title and full bibliographic details are credited, a hyperlink and/or URL is given for the original metadata page and the content is not changed in any way.

Publisher's statement:

"This is an author-created, un-copyedited version of an article published in *Astrophysical Journal*. IOP Publishing Ltd is not responsible for any errors or omissions in this version of the manuscript or any version derived from it. The Version of Record is available online at <http://dx.doi.org/10.3847/0004-637X/829/2/80>

A note on versions:

The version presented here may differ from the published version or, version of record, if you wish to cite this item you are advised to consult the publisher's version. Please see the 'permanent WRAP URL' above for details on accessing the published version and note that access may require a subscription.

For more information, please contact the WRAP Team at: wrap@warwick.ac.uk

SIMULATIONS OF ALFVÉN AND KINK WAVE DRIVING OF THE SOLAR CHROMOSPHERE - EFFICIENT HEATING AND SPICULE LAUNCHING.

C. S. BRADY AND T. D. ARBER

Centre for Fusion, Space and Astrophysics University of Warwick, Coventry, CV4 7AL, UK

(Dated: Submitted July 14, 2016)

ABSTRACT

Two of the central problems in our understanding of the solar chromosphere are how the upper chromosphere is heated and what drives spicules. Estimates of the required chromospheric heating, based on radiative and conductive losses suggest a rate of $\sim 0.1 \text{ erg cm}^{-3} \text{ s}^{-1}$ in the lower chromosphere dropping to $\sim 10^{-3} \text{ erg cm}^{-3} \text{ s}^{-1}$ in the upper chromosphere (Avrett (1981)). The chromosphere is also permeated by spicules, higher density plasma from the lower atmosphere propelled upwards at speeds of $\sim 10\text{--}20 \text{ km s}^{-1}$, for so called Type-I spicules (Pereira et al. (2012); Zhang et al. (2012)), reaching heights of $\sim 3000\text{--}5000 \text{ km}$ above the photosphere. A clearer understanding of chromospheric dynamics, its heating and the formation of spicules, is thus of central importance to solar atmospheric science. For over thirty years it has been proposed that photospheric driving of MHD waves may be responsible for both heating and spicule formation. This paper presents results from a high-resolution MHD treatment of photospheric driven Alfvén and kink waves propagating upwards into an expanding flux tube embedded in a model chromospheric atmosphere. We show that the ponderomotive coupling from Alfvén and kink waves into slow modes generates shocks which both heat the upper chromosphere and drive spicules. These simulations show that wave driving of the solar chromosphere can give a local heating rate which matches observations and drive spicules consistent with Type-I observations all within a single coherent model.

1. INTRODUCTION

The mechanisms by which the solar chromosphere are heated are still the subject of active debate. Alfvén waves have been proposed as a possible heating mechanism (Osterbrock 1961; van Ballegoijen et al. 2011) and observations show that there is enough Alfvén wave energy generated in the convection zone (De Pontieu et al. 2007) to heat the chromosphere. Previous work has examined this problem numerically. The coupling of circularly polarized Alfvén waves to magneto-acoustic modes and shocks has been studied since the 1970's by Hollweg (Hollweg 1978, 1981; Hollweg et al. 1982), and this was later extended to include white noise drivers in 1.5D (Kudoh & Shibata 1999) or 2.5D (Matsumoto & Suzuki 2012), (Matsumoto & Suzuki 2014). While these simulations do address chromospheric heating, they were mainly concerned with the upper atmosphere and solar wind and so they generally do not present detailed results for chromospheric heating. Arber et al. (2016) showed from 1D MHD simulations that chromospheric heating from Alfvén waves is primarily due to shock heating from slow mode shocks generated by ponderomotive coupling. The ponderomotive force here is defined as the non-linear force generated by the gradient in the magnetic component of MHD wave energy. Here the ponderomotive force density F_{pm} is defined by $F_{pm} = -\nabla(B_{\perp}^2)/\mu_0$, where B_{\perp} is the perturbation to the background magnetic field perpendicular to the equilibrium field Verwichte (1999).

There is a comparable history of numerical work on the possible ways in which spicules can be launched. Haerendel (1992) posited that they could be launched by ion-neutral collision effects, although the work of James & Erdelyi (2002) showed from 1D MHD simulations that this is unlikely. De Pontieu et al. (2004) simulated the launching of spicules from the non-linear interactions of acoustic waves with a 2D solar atmosphere using a reduced model, finding that it is possible to explain spicule launching by this mechanism. Murawski & Zaqarashvili (2010) and Murawski et al. (2011) found from full 2D simulations that impulsive acoustic driving can lead to the formation of spicules. Cranmer & Woolsey (2015) studied 1D simulations of spicule launching due to ponderomotive steepening of Alfvén waves, also using a reduced model, finding that this mechanism can also produce realistic spicules.

Full 3D radiation-hydrodynamic simulations of the chromosphere, such as those using the BiFROST code (Carlsson et al.

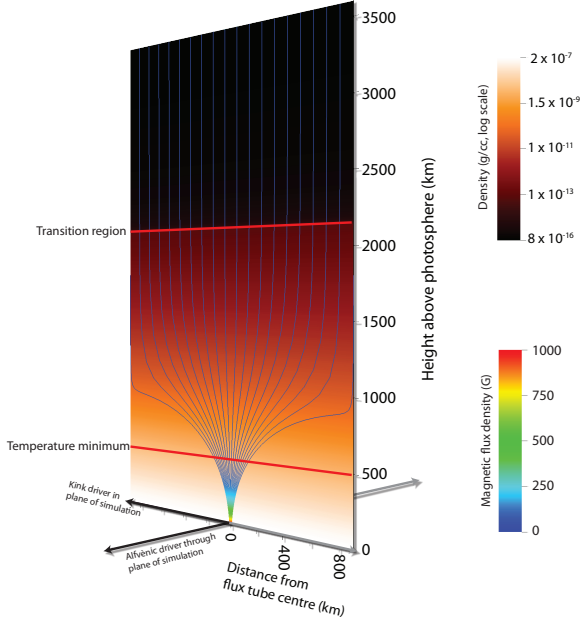


Figure 1. Magnetic field configuration and strength in the initial conditions (coloured field lines). Also shown is initial density (orange coloured plot). The direction of the two drivers used in the simulations is highlighted on the bottom boundary.

2016), have shown the presence of shocks in the chromospheric cavity. Also recent simulations of the whole chromosphere, transition region, corona and solar wind (Matsumoto & Suzuki 2012) demonstrate the importance of shocks below the transition region. However the complexity of these simulations has so far prevented a clear understanding of the underlying process as to how these shocks are formed and their precise role in matching the chromospheric heating requirements as a function of height. In this paper we present high-resolution simulations demonstrating that for a range of physically plausible parameters one can simultaneously produce chromospheric heating profiles and launch Type-I spicules with the correct length-scales, rise velocities and transverse oscillations. For each of these (heating, spicule formation and oscillation) we compare the results with observations demonstrating that MHD wave driving of the solar chromosphere can self-consistently and accurately match these observations.

2. METHOD

The aim of this paper is to evaluate the heating rate of the solar chromosphere combined with the properties of any spicules launched into the corona associated with the heating. This is achieved by simulating the interaction of a spectrum of MHD waves propagating up into a 2.5D solar atmosphere model including partial ionisation, stratification and flux tube expansion. The code used is *Lare2d* (Arber et al. 2001). A fluid equilibrium is constructed by setting up the Avrett and Loeser C7 temperature profile (Avrett & Loeser 2008) and then integrating the density from the bottom boundary so that the atmosphere is in hydrostatic equilibrium. The domain extends 9Mm above the photosphere with a transverse width of 1.8 Mm and the results presented in this paper use a resolution of 4096 cells in the vertical (y) direction and 2048 horizontally (the x direction). The position the centre of the flux patch is at $x = 0$ and $y = 0$, the base of the model photosphere, is 500 km below the temperature minimum. Throughout this paper 'height above the photosphere' refers to height above $y = 0$. Convergence is tested by repeating a sample of simulations with double the resolution showing that results presented here are accurate to within 1% on doubling the resolution. The simulation is run for a time of 1000 seconds, approximately 15 Alfvén transit times across the chromosphere, at which point it is found that the heating rate is converged.

The ionisation state is calculated from a two level Athay potential model (Leake et al. (2005), Thomas & Athay (1961)) with the ionisation state and density being iterated until the atmosphere is in hydrostatic equilibrium. A potential magnetic field is constructed numerically by solving Laplace's equation ($\nabla^2\phi = 0$) for ϕ , the magnetic scalar potential, subject to boundary conditions of transverse periodicity and a 10km flux patch on the photosphere resulting from setting $\phi = \phi_0 \exp(-x^2/\sigma^2)$ on the lower boundary with $\sigma = 10$ km (see figure 1). The magnetic field is then normalised to give a 1kG peak field at the photosphere. The resulting coronal field is then 10G. Two polarisations of driver are used. In the first Alfvén waves are introduced by driving the bottom boundary out of the plane of the simulation and will be called an Alfvénic driver. In the second a driver velocity component in the plane of the simulation is added that drives kink waves and thus both Alfvén waves and kink waves are present

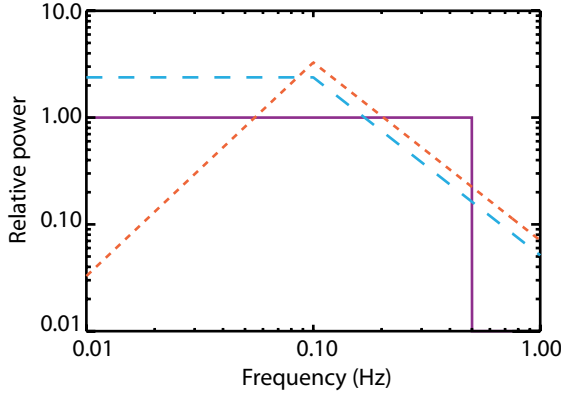


Figure 2. Power spectral density of the lower boundary driver used for the simulations. The orange dashed line is from equation 1, the blue line is equation 1 above N_1 but flat for low frequencies and the solid purple line is a flat spectra with no power-law dependence. All are normalised to give the same total Poynting flux on the lower boundary.

- this is called the mixed mode driver. Three options for the spectrum of both drivers have been tested. The first consists of a low frequency region where the power increases with k and a Kolmogorov region where power drops as $k^{-5/3}$ as in equation 1.

$$v_{z,x} = A \left(\sum_{i=0}^{N_1} \omega_i^1 \sin(\omega_i t + \phi_i) + \sum_{i=N_1}^N \omega_i^{-5/6} \sin(\omega_i t + \phi_i) \right) \quad (1)$$

The velocity component out of the plane of the simulation, v_z , is associated with an Alfvénic perturbations. v_x is the velocity component in the plane of the simulation and is only present in mixed type driving. N is the total number of frequencies combined to produce the driver spectrum and N_1 is the number of frequencies before the maximum in the spectrum. N is a large enough number to ensure that the spectrum is reproduced smoothly and that further increase in N doesn't lead to changes in the heating rate of greater than 1%. N is typically set to 5,000 in these simulations. ω_i is the frequency of spectral component i and is logarithmically spaced in the range 0.01Hz - 1 Hz. $N_1 = 0.1$ Hz for all simulations. ϕ_i is the phase for spectral component i and is selected randomly for the v_z component. For v_x , when present, its phase is the phase of v_z rotated by 90 degrees. The amplitude A is selected for most simulations to give a Poynting flux averaged across the whole bottom boundary of 2×10^7 ergs $\text{cm}^{-2} \text{s}^{-1}$. A similar driver has previously been used in (Tu & Song 2013). For the mixed driver the use of a single amplitude A ensures equal power input to both the Alfvénic and kink wave components. Other simulations are run with driver Poynting fluxes of 1×10^8 ergs $\text{cm}^{-2} \text{s}^{-1}$ and 4×10^6 ergs $\text{cm}^{-2} \text{s}^{-1}$ to evaluate the effect of the driver amplitude on the heating rate. To assess the robustness of the results to choice of driver some simulations were repeated with a flat driving spectrum up to N_1 followed by a Kolmogorov power law, as in equation 1, for higher frequencies. Also tested was a flat spectrum with no power-law dependence, see figure 2. In results where the different drivers are compared the amplitudes are always adjusted so that the total driver Poynting fluxes through the lower boundary are equal.

An isotropic 2D Kolmogorov spectrum will have $E(k)dk \sim v_k^2 k dk$ in the inertial range. For the purely Alfvén wave driver the k-vector is field aligned and for the simulated flux tube this is vertical and thus the spectrum $E(k) dk = v_k^2 dk$ is used as it would be in 1.5D. For the mixed mode driver there is a component of the driven wave spectrum k-vector perpendicular to the field at the boundary. However the wavelength of this component is of the order of the width of the tube, i.e. 20 km, and this is therefore not in the inertial range for the driver. Thus despite being a 2.5D simulation all results use the 1.5D $v(k) \sim k^{-5/6}$ driven spectrum which will give an injected energy spectrum of $E(k) \sim k^{-5/3}$.

The highest frequencies driven into the domain are when the spectra is cut-off at 1Hz. This upper cutoff frequency was chosen based on earlier 1D work (Arber et al. 2016) where it was shown to provide a converged answer. For the atmospheric and magnetic field model used there are a minimum of 3 grid points along a 1Hz Alfvén wave at the base of the domain where the wavelength is shortest. The wavelength, and thus the number of grid points per wavelength, increase with height. Note also that there is relatively little power in these high-frequency modes, down by two order of magnitude on the main low-frequency components. Testing with a higher upper cutoff frequency, and doubled resolution, shows no change in heating rate or profile. The transverse structure of the driver is a Gaussian centered on the bottom boundary flux patch. It is given a 10km width, the same as the flux patch.

The upper boundary of the domain is open. This is implemented using a Riemann characteristic method combined with a damping region. The damping scales all components of velocity so that on each time-step the velocity calculated by the core

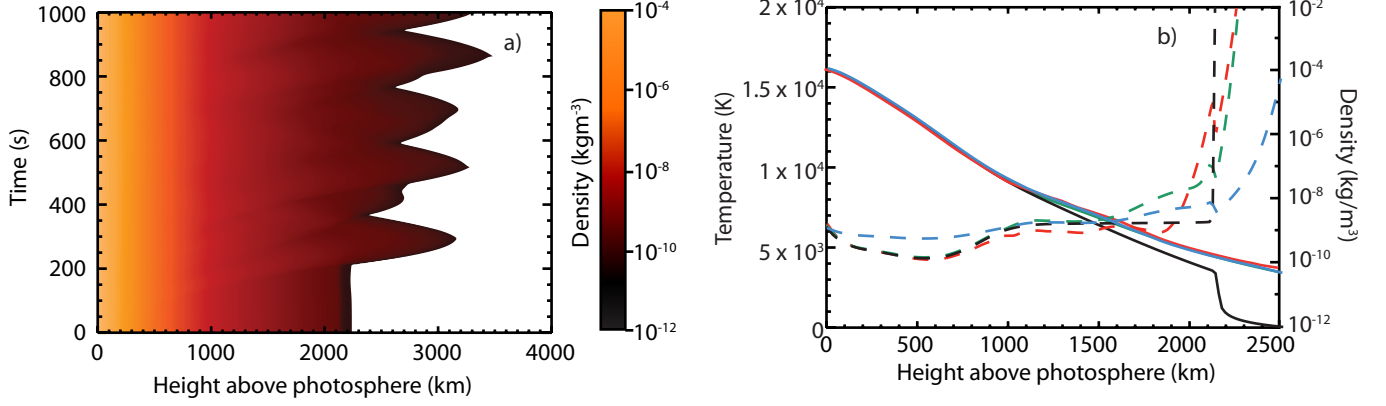


Figure 3. Change in equilibrium profiles during the simulations. (a) Time-distance plot of $\log(\text{density})$ for densities greater than $2 \times 10^{-12} \text{ kg m}^{-3}$ along the line $x = 0$. Regions of density below $2 \times 10^{-12} \text{ kg m}^{-3}$ are shown as white to emphasise the motion of the transition region. (b) Density (solid lines) and temperature (dashed lines) for different simulations averaged over the last 100 seconds of the simulation. Black is initial values, blue is the simulation including the viscous heating, red is the simulation with the cooling term and green is with no viscous heating in the simulation. All results are for the mixed driver with spectrum specified by equation 1.

solver, \mathbf{v} , is replaced by $\mathbf{v} \exp(-(y - (l_y - l_{damp}))/2l_{damp}))$ where l_y is the height of the simulation box and the damping is only applied above $l_y - l_{damp}$. l_{damp} was set to 500km in the production simulations and was tested for values between 250km and 1000km. Varying l_{damp} over this range made $< 0.1\%$ different to the heating rate at any height. Testing this boundary with discrete pulses shows that less than 0.1% of the energy incident on the upper boundary returns to the domain. The results presented here are for periodic transverse boundary conditions.

For this initial atmospheric model, magnetic field and boundary driving we solve the compressible, resistive-MHD equations in 2.5D. The resistive terms include both contributions from electron-ion plus electron-neutral collisions and the Pedersen resistivity. The Pedersen resistivity only acts on current perpendicular to the magnetic field and results from ion-neutral collisions in the partially ionised chromospheric atmosphere. Neutrals are also required to get the correct pressure scale height from the C7 model temperature. To correctly handle shocks in these simulations a compatible shock viscosity (Caramana et al. 1998) is used to ensure the correct jump conditions. This also allows measurement of the shock heating which in these simulations is entirely due to this viscosity. The heating from this shock viscosity is essential to get the entropy jump across the shock, so this heating is included in the simulation. The model does not include thermal conduction or radiative losses and thus throughout the simulation the atmosphere begins to heat up as we have the heating sources but not the losses. Further simulations are therefore run where either the shock heating is simply not included, or a cooling term is included that subtracts a running average over $\tau = 160$ seconds of the shock heating from the system. Thus the energy equation used in the simulations is,

$$\frac{D\epsilon}{Dt} = -\frac{P}{\rho} \nabla \cdot \mathbf{v} + \frac{H_{\text{visc}}}{\rho} - \frac{H_{\text{cooling}}}{\rho} \quad (2)$$

where ρ is the mass density, P is the gas pressure, \mathbf{v} is the fluid velocity, ϵ is the specific internal energy density, H_{visc} is the viscous (shock) heating and H_{cooling} is a cooling term given by

$$H_{\text{cooling}}(\mathbf{r}, t) = \frac{1}{\tau} \int_{t-\tau}^t H_{\text{visc}}(\mathbf{r}, t') dt' \quad (3)$$

This cooling term will tend, on average, to maintain the atmosphere close to its initial profile irrespective of the magnitude of the heating term. For all simulations H_{Ohmic} , total resistive heating including both electron collisional and Pedersen resistivities, is calculated for diagnostic purposes but not added to the energy equation. Throughout this paper the only heating term included in the energy equation is therefore the viscous shock heating.

3. RESULTS

The temperature and density at the start and the end of the simulations, for a variety of combinations of heating terms in equation 2, are shown in figure 3 along with a time distance plot of the density. The uplifting of denser material leads to an increase in the average density for heights 1.2 Mm above the lower boundary. This change is insensitive to the inclusion or absence of shock heating or the cooling term in equation 2. The temperature profile does change depending on the terms included in equation 2 and so the simulations below are repeated for all three cases, i.e. no heating, shock heating and shock heating plus

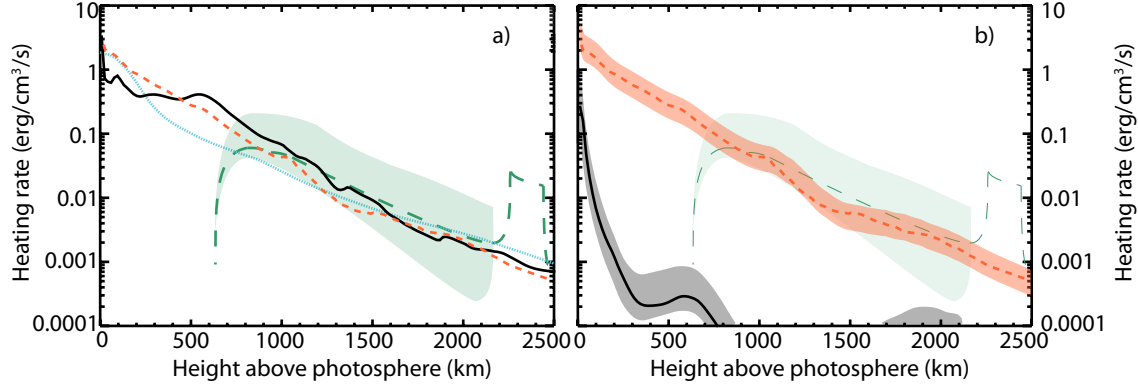


Figure 4. Heating rates as a function of height averaged across the simulation domain. On panel a) the solid black line is viscous heating from simulations with mixed mode driving. The blue dotted line is the heating from a purely Alfvénic driver. The orange short dashed line is from a simulation with a mixed mode driver including the cooling term in the energy equation. The solid black, blue dotted and orange dashed line are all from simulations which included the viscous heating in the energy equation and used the spectrum specified by equation 1. The green dashed line is the estimate of local cooling due to chromospheric radiation from Avrett (1981) Model C for the quiet chromosphere. The green shaded area is bounded by the Avrett Model A (dark network region) and Avrett Model F (very bright network element). On panel b) the orange short dashed line, green dashed line and green area are the same as in panel a). The black solid line is the resistive heating from the same simulation, and the grey and orange areas are bounded by simulations where the Poynting flux through the boundary is either increased or decreased by a factor of 5.

cooling. The primary difference between these is that the simulations which include shock heating, but not the cooling term, lead to a less steep temperature profile through the transition region as the atmosphere continues to heat and rise. In this case the majority of the additional heating goes into an increase in the gravitational potential energy.

Figure 3 b) shows that the force balance in the upper chromosphere and transition region is changed by the action of the waves. Temperature and pressure profiles change differently, so considering only gravity and static pressure forces there is a net downwards force. Despite this figure 3 a) shows that the atmosphere is still in a dynamic equilibrium state, oscillating vertically but not systematically moving up or down. The additional upwards pressure force is provided by the shock ram pressure $0.5\rho v^2$ which in the upper chromosphere is 2.5 times the static pressure, consistent with the observed shock Mach numbers.

The viscous heating rate averaged across the flux structure is shown in figure 4 a) as a black line for a mixed mode driver and a blue dotted line for the Alfvénic driver. The orange dashed line shows the effect of including the cooling term in the mixed driver simulation. Simulations for the mixed driver but without either the cooling term or viscous heating included in the energy equation produce a heating profile indistinguishable from the orange dashed line in figure 4(a) and is therefore not shown. Comparing with observed heating rates from Avrett (1981) (green dashed line and grey shaded area), the simulated heating rates are a match from 700km above the photosphere to 2100km. The driver amplitude, and hence Poynting flux, are only loosely constrained by observations to be close to $2 \times 10^7 \text{ ergs cm}^{-2} \text{ s}^{-1}$ so the effect of changing this is shown in figure 4 panel b). The orange dashed line is the same as in panel a) and the orange shaded region is the range of heating rates obtained by increasing or decreasing the driver Poynting flux by a factor of 5. The black line is the resistive heating rate, and the gray shaded region around it is the change in the resistive heating by changing the driver Poynting flux. The heating rate from the simulations are in quantitative and qualitative agreement with the observationally determined heating from Avrett (1981) between the heights of 700km and 2100km. In Avrett (1981) it is explicitly stated that "The net radiative cooling rate $\phi(h)$ throughout the chromospheric portion of each model is a direct measure of the non-radiative heating required to produce the chromospheric temperature increase.", and that the apparent temperature plateaus in the transition region in Avrett's model that are needed to reproduce the Lyman- α spectrum make interpretation of the radiative loss functions above 2 Mm difficult. The use of radiation from chromospheric lines in Avrett (1981) also mean this method cannot match heating requirements in the photosphere. Thus one would only expect the shock heating calculated here from simulations to match the results from Avrett (1981) in the range shown shaded in figure 4 between 700-2100 km.

To assess the sensitivity of the heating profiles to the choice of spectra the results for the mixed driver with viscous heating and cooling terms included in the energy equation were repeated for the three spectra shown in figure 2. These results are shown in figure 5 confirming that the precise functional form of the driving spectrum only weakly affects the heating profile. Across all driver spectra roughly 50% of the boundary driven Poynting flux emerges into the corona.

The averaged heating rates in figure 4 miss the variability of the shock heating. An example of the variability 100km below the transition region is shown in figure 6 panel (a). Here the height of the initial transition region is defined as the height at which

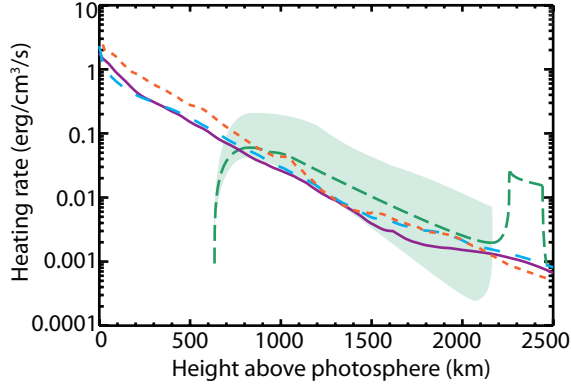


Figure 5. Heating rates as a function of height averaged across the simulation domain for various driving spectra. All results are for the mixed mode driver with shock heating and the cooling term in the energy equation. The orange dashed line is for a spectrum matching equation 1 and is the same as the orange line in figure 4. The blue line is equation 1 above N_1 but flat for low frequencies and the solid purple line is a flat spectra with no power-law dependence. Colours match those use in figure 2

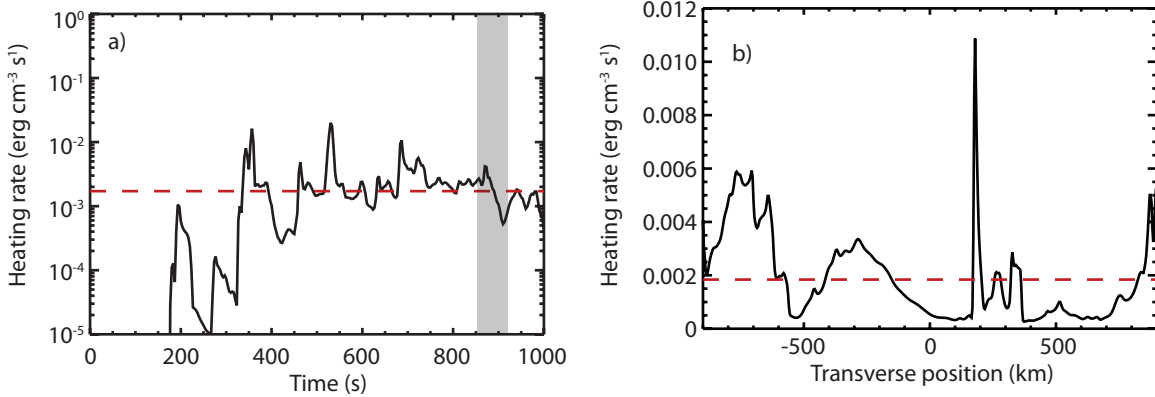


Figure 6. Panel a) shows the time history of the instantaneous heating rate at a point 100km below the initial height of the transition region at the centre of the flux structure for a simulation of a mixed mode driver with included cooling term. The red dashed line is the average heating rate for that height as shown on figure 4. Panel b) shows the transverse structure of the heating at the same height averaged over the time shown in the grey box in panel a. The red dashed line is again the average heating rate.

the initial equilibrium mass density $\rho = 10^{-11} \text{ kg m}^{-3}$, i.e. a height of 2162 km for this simulation domain. An example of the transverse structure of the heating rate averaged over the grey box in panel (a) is shown in panel (b), demonstrating that transverse structure is present in the simulation.

The origin of the heating is from shock dissipation of acoustic modes propagating along field lines. This is shown in figure 7 by the presence of the -2 power law which is characteristic of shock dominated time series. Note that while the shortest wavelength which can be resolved at $y = 0$ restricts the driver to frequencies below 1 Hz the wavelength expansion with height means that the spectrum in figure 7 extends beyond 1 Hz. The heating rates recorded in these simulations are purely those due to shock viscosity and resistivity. Heating due to resistivity is shown to be small and can be ignored. Shock viscosity goes to zero in smooth regions of the solution, and the convergence of the numerical results gives confidence that the heating is due to discontinuities, i.e. shocks. It is possible that phase mixing, that cascades down to arbitrarily small scales in the absence of bulk viscosity, may contribute to some of the heating. However the fact that the evolved velocity spectrum is that of a shock dominated time series strongly suggests that the heating is dominated by shocks. In addition the heating is strong in the centre of the flux tube, where phase-mixing would be absent. There is no acoustic component in the driver so these waves are generated from the boundary driven MHD waves. Figure 8 shows both the specific ponderomotive force and parallel compressive component of $\nabla \cdot \mathbf{v}$ for the mixed mode driver averaged across the simulation domain and the longest period in the driver. The specific ponderomotive force is defined as $(-1/\mu_0\rho)\nabla B_{\perp}^2$ where B_{\perp} is the magnetic field perturbation perpendicular to the background magnetic field.

The formation of shocks causes a lifting of dense material from the lower atmosphere (figure 9), and for the mixed mode drivers, internal reflections in the flux tube cause transverse structuring of this dense material. If a purely Alfvénic driver is used then the transverse structuring in the shock driven, uplifted material is reduced. Taking the relative density change of the plasma

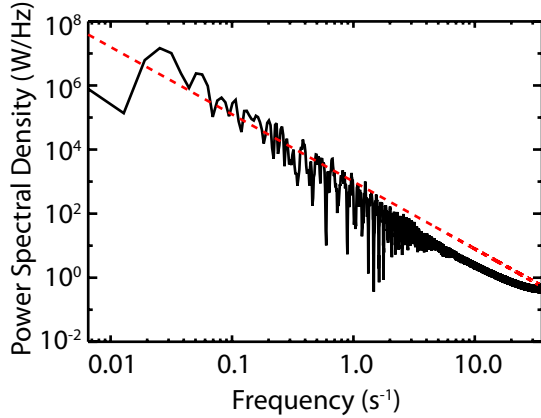


Figure 7. Power spectral density measured at a point 100km below the original location of the transition region. The red dashed line is a power law with a power of -2.

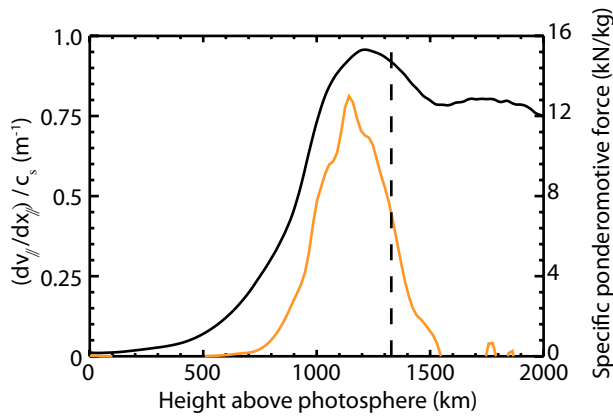


Figure 8. The specific ponderomotive force (black line) and parallel compressive component of $\nabla \cdot \mathbf{v}$ normalised to the local sound speed (orange line) for the mixed mode driver. Both are averaged across the flux tube at fixed height and over the longest period of the boundary driver. The vertical line is the location of the $\beta = 1$ surface.

in the simulation and overplotting it on an example observational picture of spicules produces a strong visual similarity, so these density structures can be preliminarily described as spicules. These spicules are carried up to a height of $\sim 2500 - 4000$ km above the photosphere. The rise speed of spicules is not the local fluid speed as these are propagating shocks. The rise speed is therefore calculated by tracking the location of the reference transition region mass density $\rho = 10^{-11} \text{ kg m}^{-3}$ for rising spicules. The mean rise speed across all spicules was $\sim 12 \text{ km s}^{-1}$. A representative spicule is shown in figure 10 (a) for which the peak rise speed is 30 km s^{-1} and the average rise speed 15 km s^{-1} . The range of maximum rise speeds across all spicules is $24 - 32 \text{ km s}^{-1}$ and the range of average rise speeds is $10 - 15 \text{ km s}^{-1}$. Both the height and the rise speed are comparable with observations (1000-10000km above the photosphere and 15-65km/s including both Type I and Type II spicules. These results best match Type I spicules.) (Beckers (1968), Pasachoff et al. (2009), Pereira et al. (2012)). Recording the out-of-plane velocity at the transition region (figure 10 b), transverse oscillations are measured with an r.m.s. speed of $\sim 9 \text{ km s}^{-1}$ for the mixed driver again consistent with observations (De Pontieu et al. (2007); Zhang et al. (2012)).

The results are qualitatively in agreement with the results of Matsumoto & Suzuki (2014) who briefly discuss heating of the chromosphere in their section 6.1. They find that heating below the transition region is dominated by shock heating and identify both fast and slow shocks as being important. The overall heating rates in Matsumoto & Suzuki (2014) are comparable to those presented here but due to the the low resolution in the chromosphere used in those simulations Matsumoto & Suzuki (2014) point out that their code produces strong numerical heating. The results presented in this manuscript are fully converged.

4. CONCLUSIONS

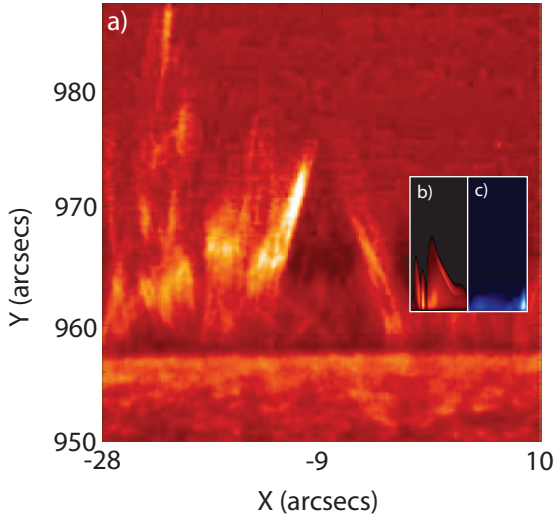


Figure 9. Comparison of observed and simulated spicules. The observation is from an Hinode SOT Ca II H image showing spicules taken on April 29th at 0224UT from [Tsiropoula et al. \(2012\)](#). The insert plots are the relative change in density from the initial conditions of the coronal part of a simulation at the same height and scale. The red coloured insert (b) is for the mixed mode driver and the blue insert (c) for the purely Alfvénic driver.

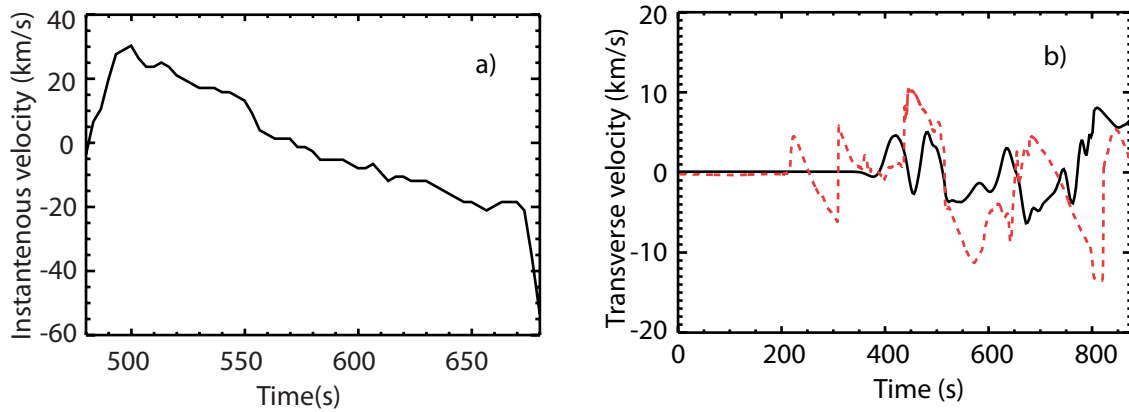


Figure 10. a) Instantaneous vertical velocity of a spicule measured as the speed of mass density $\rho = 10^{-11} \text{ kg m}^{-3}$ b) Transverse velocity (out of the simulation plane) measured at transition region height from the centre of the flux tube. The solid line is for the Alfvénic driver and the red dashed line the mixed driver.

This letter presents the results from 2.5D simulations of MHD wave driven heating of the chromosphere which also show spicule launching. They show that by choosing plausible values for the driver amplitude and spectrum, magnetic field and atmosphere model robust heating rates comparable to observations are obtained. Self-consistently with this, spicule like blobs of enhanced density are launched into the corona with average rise speeds of $\sim 12 \text{ km s}^{-1}$, peak rise speeds in the range $24 - 32 \text{ km s}^{-1}$. These spicules have transverse oscillations with r.m.s. velocities of $\sim 9 \text{ km s}^{-1}$. All of these numbers are consistent with observations. If a mixed kink and Alfvén type driver is specified then realistic transverse structuring of the driven spicules is also observed. From the simulations presented here we conclude:

- For drivers which are either Alfvén waves or mixed Alfvén and kink waves, provided the Poynting flux is kept near $\sim 2 \times 10^7 \text{ erg cm}^{-2} \text{ s}^{-1}$, these waves can heat the upper chromosphere.
- This heating is from shock dissipation of slow modes generated by the ponderomotive force.
- The heating is insensitive to the upper cut-off in driver spectrum or profile across the three spectra tested.

- Compressibility is essential for modelling the chromosphere and an Alfvén wave driver does not lead to a turbulent cascade to dissipation scales but instead loses energy by coupling to slow modes.
- If a mixed mode driver is specified internal reflection within the flux tube generates transverse structure higher up similar to that observed in spicules.
- The rise of dense material has a velocity consistent with Type-I spicules.
- The transverse oscillations have peak and RMS velocities comparable to observations.

These simulations are limited to 2.5D. The fastest Alfvén wave cascade in Alfvénic turbulence requires wave-vector matching in 3D. It is therefore possible that in 3D a turbulent cascade terminated by resistive damping will be a more efficient heating mechanism. However, given that shock heating is orders of magnitude more important than resistive in 2D, and 3D effects will not turn off shock heating, shock heating is still likely to remain an important heating mechanism in 3D.

The model used in this paper does not attempt to accurately describe the non-local transport of energy through radiation or non-LTE physics. These are surely important for predicting observational signatures of chromospheric spectral lines. Despite this the heating rates and spicule properties have converged before the simulation ends and the coupling of MHD waves to slow modes via the ponderomotive force depends only on the magnetic field and local mass density. This mechanism is robust in that the ponderomotive force depends on only the gradient of the MHD wave magnetic field energy which in turn acts on the local chromospheric mass density. This occurs low in the atmosphere where the ion-neutral coupling is strong and hence all that matters is the MHD wave energy, its spectrum, and the local mass density. Once these waves are generated they will shock due to density stratification in the upper atmosphere - thereby heating the chromosphere. As such, it seems likely that the results presented here would be reproduced in a full radiation hydrodynamic, non-LTE simulation of the same shock resolution. These results show that both the qualitative and quantitative properties of chromospheric heating and Type-I spicules can be produced from the same underlying physical process: the ponderomotive formation of shocks from transverse photospheric motion.

ACKNOWLEDGEMENTS

This work used the Darwin Data Analytic system at the University of Cambridge, operated by the University of Cambridge High Performance Computing Service on behalf of the STFC DiRAC HPC Facility (www.dirac.ac.uk). This equipment was funded by a BIS National E-infrastructure capital grant (ST/K001590/1), STFC capital grants ST/H008861/1 and ST/H00887X/1, and DiRAC Operations grant ST/K00333X/1. DiRAC is part of the National E-Infrastructure.

This work used the DiRAC Data Centric system at Durham University, operated by the Institute for Computational Cosmology on behalf of the STFC DiRAC HPC Facility (www.dirac.ac.uk). This equipment was funded by a BIS National E-infrastructure capital grant ST/K00042X/1, STFC capital grant ST/K00087X/1, DiRAC Operations grant ST/K003267/1 and Durham University. DiRAC is part of the National E-Infrastructure.

REFERENCES

- Arber, T. D., Brady, C. S., & Shelyag, S. 2016, *Astrophysical Journal*, 817, 94
- Arber, T. D., Longbottom, A. W., Gerrard, C. L., & Milne, A. M. 2001, *Journal of Computational Physics*, 171, 151
- Avrett, E. H. 1981, *Proc. Advanced Study Institute, Solar Phenomena in Stars and Stellar Systems*, 173
- Avrett, E. H., & Loeser, R. 2008, *Astrophysical Journal Supplement Series*, 175, 229
- Beckers, J. M. 1968, *Solar Physics*, 3, 367
- Caramana, E. J., Shashkov, M. J., & Whalen, P. P. 1998, *Journal of Computational Physics*, 144
- Carlsson, M., Hansteen, V. H., Gudiksen, B. V., Leenaarts, J., & Pontieu, B. D. 2016, *Astronomy and Astrophysics*, 585
- Cranmer, S., & Woolsey, L. 2015, *Astrophysical Journal*, 812, 71
- De Pontieu, B., Erdelyi, R., & James, S. 2004, *Nature*, 430, 536
- De Pontieu, B., McIntosh, S. W., Carlsson, M., et al. 2007, *Science*, 318, 1574
- Verwichte, E., Nakariakov, V. M. & Longbottom, A. W., 1999, *J. Plasma Physics*, 62, 219
- Haerendel, G. 1992, *Nature*, 360, 241
- Hollweg, J. 1978, *Solar Physics*, 56, 305
- Hollweg, J., 1981, *Solar Physics*, 70, 25
- Hollweg, J., Jackson, S., & Galloway, D. 1982, *Solar Physics*, 72
- James, S. P., & Erdelyi, R. 2002, *Astronomy and Astrophysics*, 393, L11
- Kudoh, T., & Shibata, K. 1999, *Astrophysical Journal*, 512, 493
- Leake, J. E., Arber, T. D., & Khodachenko, M. L. 2005, *Astronomy and Astrophysics*, 442, 1091
- Matsumoto, T., & Suzuki, T. K. 2012, *Astronomy and Astrophysics*, 749, 8
- Matsumoto, T., & Suzuki, T. K. 2014, *Monthly Notices of the Royal Astronomical Society*, 440, 2, 971
- Murawski, K., Srivastava, A. K., & Zaqarashvili, T. V. 2011, *Astronomy and Astrophysics*, 535, A58
- Murawski, K., & Zaqarashvili, T. V. 2010, *Astronomy and Astrophysics*, 519, A8
- Osterbrock, D. 1961, *Astrophysical Journal*, 134, 347
- Pasachoff, J. M., Jacobson, W. A., & Sterling, A. C. 2009, *Solar Physics*, 260, 59

- Pereira, T. M. D., De Pontieu, B., & Carlsson, M. 2012, *Astrophysical Journal*, 759, 18
- Thomas, & Athay. 1961, *Physics of the Solar Chromosphere* (3rd ed) (Oxford University Press)
- Tsiropoula, G., Tziotziou, K., Kontogiannis, I., et al. 2012, *Space Science Reviews*, 169
- Tu, J., & Song, P. 2013, *Astrophysical Journal*, 777, 53
- van Ballegoijen, A. A., Asgari-Targhi, M., Cranmer, S. R., & DeLuca, E. E. 2011, *Astrophysical Journal*, 736, 3
- Zhang, Y. Z., Shibata, K., Wang, J. X., et al. 2012, *Astrophysical Journal*, 750